Development and Testing of Polar Weather Research and Forecasting (WRF) Model. Part I: Greenland Ice Sheet Meteorology*

KEITH M. HINES

Polar Meteorology Group, Byrd Polar Research Center, The Ohio State University, Columbus, Ohio

DAVID H. BROMWICH

Polar Meteorology Group, Byrd Polar Research Center, and Atmospheric Sciences Program, Department of Geography, The Ohio State University, Columbus, Ohio

(Manuscript received 5 December 2006, in final form 31 July 2007)

ABSTRACT

A polar-optimized version of the fifth-generation Pennsylvania State University–National Center for Atmospheric Research Mesoscale Model (MM5) was developed to fill climate and synoptic needs of the polar science community and to achieve an improved regional performance. To continue the goal of enhanced polar mesoscale modeling, polar optimization should now be applied toward the state-of-the-art Weather Research and Forecasting (WRF) Model. Evaluations and optimizations are especially needed for the boundary layer parameterization, cloud physics, snow surface physics, and sea ice treatment. Testing and development work for Polar WRF begins with simulations for ice sheet surface conditions using a Greenland-area domain with 24-km resolution. The winter month December 2002 and the summer month June 2001 are simulated with WRF, version 2.1.1, in a series of 48-h integrations initialized daily at 0000 UTC. The results motivated several improvements to Polar WRF, especially to the Noah land surface model (LSM) and the snowpack treatment. Different physics packages for WRF are evaluated with December 2002 simulations that show variable forecast skill when verified with the automatic weather station observations. The WRF simulation with the combination of the modified Noah LSM, the Mellor–Yamada–Janjić boundary layer parameterization, and the WRF single-moment microphysics produced results that reach or exceed the success standards of a Polar MM5 simulation for December 2002. For summer simulations of June 2001, WRF simulates an improved surface energy balance, and shows forecast skill nearly equal to that of Polar MM5.

1. Introduction

The climatic significance of the polar regions is highlighted by "polar amplification," that is, increased climate sensitivity at these latitudes due to factors such as the sea ice–albedo feedback (Manabe and Stouffer 1980; Holland and Bitz 2003; McBean et al. 2004). There is a large range in the warming at high latitudes in both hemispheres simulated by global climate models in response to increasing CO_2 concentrations, with the largest range on earth located in the Arctic (Houghton et al. 2001). Furthermore, the polar regions play a critical role in global sea level variations resulting from the mass balance of the Greenland and Antarctic ice sheets (e.g., Wild et al. 2003; Rignot and Kanagaratnam 2006). One approach to quantitatively evaluate the various physical processes active in the Arctic and Antarctic is numerical integrations with regional climate models that typically have higher horizontal resolution depictions of the topography and surface features. Furthermore, the model physics can be optimized so as to be robust for the key regional processes and mechanisms. This is especially important as the polar regions are frequently not prioritized for the development of model parameterizations (e.g., Kattsov et al. 2004). For example, excessive cloud cover was found to be a persistent problem over the Antarctic in sensitivity simulations using an earlier-generation mesoscale model (Hines et al. 1997a,b), similar to results found by Man-

* Byrd Polar Research Center Contribution Number 1361.

Corresponding author address: Keith M. Hines, Polar Meteorology Group, Byrd Polar Research Center, The Ohio State University, 1090 Carmack Road, Columbus, OH 43210-1002.
E-mail: hines.91@osu.edu

DOI: 10.1175/2007MWR2112.1

ning and Davis (1997) for cold, high clouds over the continental United States.

In response to the Arctic's importance for climate change, the Study of Environmental Arctic Change (SEARCH) project is conducting extensive, interdisciplinary, multiscale studies of high northern latitudes (Overland et al. 2003). As a way of integrating observations and modeling efforts into a comprehensive picture of the climate and synoptic meteorology of the Arctic, SEARCH includes plans for a multiyear reanalysis from all available remote sensing and in situ data. This Arctic System Reanalysis (ASR) will require an Arctic-friendly atmospheric numerical model with state-of-the-art dynamics and polar physics. Fortunately, extensive earlier work with Arctic and Antarctic domains provides a basis for regional high-resolution simulations (e.g., Lynch et al. 1995; Heinemann 1997; van Lipzig et al. 1999; Bromwich et al. 2001; Cassano et al. 2001; Klein et al. 2001). Earlier mesoscale modeling work with a polar-optimized model is discussed in section 2. Section 3 of this paper describes the Weather Research and Forecasting Model (WRF) and its polar modifications. Section 4 specifies the Greenland domain and data sources. Section 5 shows the results of wintertime December 2002 simulations. Simulations of an early summer month, June 2001, are presented in section 6. Summary and conclusions are given in section 7.

2. Polar MM5

Previously, the fifth-generation Pennsylvania State University–National Center for Atmospheric Research (NCAR) Mesoscale Model (MM5; Dudhia 1993; Grell et al. 1995) was adapted for use in polar regions. The model (referred to as Polar MM5) was optimized at The Ohio State University in collaboration with the Mesoscale and Microscale Meteorology (MMM) Division at NCAR and implemented into the MM5 community modeling system managed by NCAR. The polar-optimized MM5 demonstrated a much improved regional performance (e.g., Bromwich et al. 2001; Cassano et al. 2001). In addition to climate applications for the modern Arctic (Arctic Rivers; Serreze et al. 2003) and Antarctic (Guo et al. 2003; Bromwich et al. 2004) and paleoclimate applications for the Last Glacial Maximum (Bromwich et al. 2005b), Polar MM5 generates the high-resolution numerical forecasts of Antarctic Mesoscale Prediction System (AMPS; Bromwich et al. 2003; Powers et al. 2003) in support of operational and logistic needs of the United States Antarctic Program. Furthermore, Box et al. (2006) recently used Polar MM5 runs calibrated by independent in situ observations to demonstrate coherent regional patterns of Greenland ice sheet surface mass balance change over a recent 17-yr period (1988–2004). Their calculations indicate the Greenland ice cap provides the largest individual glacial contribution to recent global sea level rise.

The Polar MM5 development included the following modifications: (i) improvements to the cloud microphysics by replacing the Fletcher (1962) equation for ice nuclei concentration with that of Cooper (1986); (ii) use of the NCAR Community Climate Model, version 2, radiation scheme with the radiative properties of clouds determined from the predicted cloud water and ice mixing ratios of the Reisner explicit microphysics parameterization (Reisner et al. 1998); (iii) use of the latent heat of sublimation for calculations of latent heat flux over ice surfaces and assumption of ice saturation when calculating surface saturation mixing ratios over ice; (iv) improved treatment of heat transfer through snow–ice surfaces including an increase in the number of substrate levels from six to eight allowing a resolved substrate depth of 1.91 m; (v) optimized boundary layer parameterization with turbulent fluxes in the atmosphere and near the surface taken from the 1.5-order turbulence closure used in the National Centers for Environmental Prediction (NCEP) Eta Model (Janjić 1994); and (vi) introducing a separate sea ice category with specified thermal properties and open water fraction.

As the final standard version of MM5 has been released, and it is no longer a primary vehicle for future mesoscale model development, a next goal is optimizing the new, state-of-the-art WRF (see http://wrf-model.org) for a variety of polar applications. Following the path of development for Polar MM5, evaluations and optimizations are especially needed for boundary layer parameterization, cloud physics and cloud-radiative processes, snow surface physics, and sea ice treatment for the polar version of WRF (Polar WRF). Developmental simulations should be performed for at least three regimes of polar climate: (i) ice sheet surfaces (Antarctica and Greenland), (ii) polar oceans (especially sea ice domains), and (iii) Arctic land (tundra and boreal forest, for example). This paper concentrates on the first with Greenland-area simulations. Development of Polar WRF for ocean and land surfaces will be detailed in subsequent publications.

3. Polar WRF

The WRF mesoscale modeling system was recently developed by a planned multiagency collaboration to improve simulation accuracy over a range of spatial

scales down to that of individual clouds, with increased emphasis on horizontal scales of 1–10 km. The Advanced Research WRF (ARW) is a modular, nonhydrostatic model with conservative properties designed for both research and operational applications (Skamarock et al. 2005) with improved software (Michalakes et al. 1999, 2004). The model is integrated in time with a third-order Runge–Kutta scheme with smaller time steps for acoustic waves and gravity waves. Model variables are horizontally staggered on an Arakawa grid-C, and the model top is a constant pressure surface. Similar to MM5, multiple nested grids with one- or two-way interaction are possible. The data assimilation capabilities of the WRF-Var program are adapted from MM5 3DVAR (Barker et al. 2003, 2004). Multiple physics package options allow flexibility in treating the earth surface, atmospheric boundary layer, shortwave and longwave radiation, explicit cloud physics, and subgrid-scale cumulus.

Version 2.1.1 of the ARW, released by NCAR on 9 November 2005, is employed for WRF simulations in this paper. All WRF simulations reported here have 28 terrain-following sigma layers between the earth's surface and the model top at 10 hPa. The top is set at a high level for better treatment of upward-propagating gravity waves generated by high ice sheet topography (e.g., Guo et al. 2003; Bromwich et al. 2005a). Highest vertical resolution is in the boundary layer with the lowest 10 layers over Greenland are centered at approximately 14, 42, 75, 118, 171, 238, 325, 433, 561, and 748 m, respectively, AGL. The output fields every 6 h from NCEP's Global Forecast System (GFS; Caplan and Pan 2000), formerly known as the Aviation (AVN) model, provide the specified initial and boundary conditions. The time step is 60 s, and subgrid-scale cumulus is parameterized with the Kain–Fritsch scheme. For longwave radiation, the Rapid Radiative Transfer Model (RRTM; Mlawer et al. 1997) option is applied. The RRTM alleviates the deficit in downward longwave radiation for clear-sky conditions present in many earlier radiation schemes (e.g., Pinto et al. 1997).

An important consideration for Polar WRF is the selection of physical parameterizations best suited for polar conditions. Hence, it was necessary to test different options for cloud physics, shortwave radiation, surface treatment and the planetary boundary layer (PBL). For cloud physics, the WRF single-moment 5-class (WSM5; Hong et al. 2004) parameterization includes prognostic equations for cloud water, cloud ice, rain, snow, and water vapor. Furthermore, the diagnostic relation for ice number concentration depends on *ice mass content* rather than temperature. The more advanced option, the Thompson et al. (2004) *2-moment*, 6-class scheme is developed from the earlier Reisner et al. (1998) scheme of MM5. The new scheme includes prognostic graupel and predicted ice number concentration. Shortwave radiation is represented by the Goddard scheme with 11 spectral bands that accounts for both diffuse and direct solar radiation (Chou and Suarez 1994).

A more advanced version of the Thompson et al. (2004) and two-moment microphysics scheme was supplied by G. Thompson for the Polar WRF simulations. A critical new feature is an adjustable condensation nuclei concentration. Based on a suggestion by H. Morrison (2006, personal communication) we reduced the nuclei concentration, as Greenland has a relatively pristine atmosphere (e.g., Heidam et al. 1999). The original concentration 1×10^8 m^{-3} was reduced to 2×10^7 m^{-3}. Furthermore, the Penman–Monteith equation for evapotranspiration was updated for frozen surfaces. For snow, permanent ice, and sea ice at subfreezing temperatures, surface saturation vapor pressure is now computed with respect to ice rather than liquid water, following Mahrt and Vickers (2005).

For the boundary layer, the Yonsei University (YSU; Hong et al. 2006) scheme is the successor to MM5's Medium-Range Forecast Model PBL (Hong and Pan 1996), and it is run in conjunction with a similarity-based scheme for surface exchange coefficients. The YSU PBL top is determined from a critical bulk Richardson number set at zero. The scheme includes updates to the entrainment, and countergradient fluxes due to nonlocal gradients are allowed. Another PBL option is the eta scheme, also known as the Mellor–Yamada–Janjić (MYJ) scheme, run in conjunction with the eta surface layer scheme also based on similarity theory (Janjić 1996, 2002). The MYJ PBL includes a nonsingular implementation of level 2.5 Mellor–Yamada closure for turbulence in the PBL and free atmosphere.

The land surface is treated with either the 4-layer Noah land surface model (LSM) or the 6-layer Rapid Update Cycle (RUC) LSM. The RUC scheme includes frozen soil, fractional snow cover, and up to two snow layers (Smirnova et al. 1997, 2000). The LSM now commonly referred to as Noah, the name evolved from the earlier acronym NOAH combining NCEP, Oregon State University, Air Force, and Hydrologic Research Laboratory, is based on the Oregon State University LSM (Chen and Dudhia 2001) and includes predicted soil ice, and fractional snow cover characteristics. Four prognostic substrate layers are 0.1, 0.3, 0.6, and 1 m thick, with a time-constant temperature given at a depth of 8 m. Oceanic grid points are treated as open water or 100% sea ice for locations with less than or

greater than 50% sea ice coverage, respectively, in the provided initial data. The fixed temperature below the sea ice is set at 271.4 K.

Preliminary simulations with WRF suggested several improvements to the Noah LSM treatment of the Greenland ice sheet. The linearized surface energy balance equation solved for the skin temperature analogous to Mahrt and Ek's (1984) Eq. (7) with upward longwave flux a function of the lowest atmospheric temperature, was replaced with an iterative solution to the full surface energy balance equation,

$$H\frac{\partial T_s}{\partial t} = \varepsilon[L(\downarrow) - \sigma T_s^4] + (1 - \alpha)S(\downarrow) - H_s(T_s) - L_s + G(T_s) + Q, \quad (1)$$

where H is the heat capacity associated with the skin temperature T_s, t is time, ε is surface emissivity, $L(\downarrow)$ is downward longwave radiation, σ is the Stefan–Boltzmann constant, α is surface albedo, $S(\downarrow)$ is downward shortwave radiation, H_s is the sensible heat flux, L_s is the latent heat flux, G is the ground heat flux upward to the surface, and Q represents other diabatic processes including phase change and heat flux by precipitation. The upward longwave flux is now a function of the skin temperature, which can be much colder than the boundary layer atmospheric temperature during winter. The solution is obtained by taking T_s as representing an infinitely thin layer, thus H and the lhs are zero. In contrast, the lowest atmospheric level and the uppermost "soil" level (which can now include the snowpack) are both prognostic and have finite depths and heat capacities, so heat capacity is accounted for above and below the surface. Upward longwave radiation, sensible heat flux and ground heat flux are adjusted through T_s until balance is achieved. Ground heat flux is computed from

$$G = \frac{D}{\Delta z}(T_{\text{soil}} - T_s), \quad (2)$$

where D is the thermal conductivity of snow, T_{soil} is temperature of the upper "soil" layer, and Δz is the depth of the midpoint of the upper subsurface layer. Furthermore, longwave emissivity for snow and ice is increased to 0.98. The result is a highly improved conservation of energy and a closer match to temperature observations.

Furthermore, to improve the heat transfer between the snowpack and the atmosphere the maximum depth of the top snow cover layer, included in Δz, is set at the depth of the upper subsurface layer. Hence, a deep snowpack will effectively be treated with multiple prognostic subsurface layers, rather than as an extra layer on top of the prognostic subsurface layers. Additionally, we modify the density, heat capacity, and heat conductivity of the snowpack based on Yen's (1981) observations of Antarctic snow firn properties, consistent with Polar MM5's treatment of subsurface heat. Albert and Shultz (2002) show vertical profiles of firn density at Summit, Greenland, and the values are similar to those of Yen's Antarctic profiles. Furthermore, for permanent ice surfaces or 100% snow cover surfaces with the top layer surface temperature colder than -5°C, the top layer thermal conductivity, 0.108 W m^{-1}K^{-1}, is calculated by WRF based on a snow density of 200 kg m^{-3}. From Yen's (1981) data we also set the volumetric heat capacity of Greenland permanent ice at 0.817×10^6, 0.855×10^6, 0.923×10^6, and 1.010×10^6 J m^{-3}K^{-1} for the Noah layers centered at 0.05-, 0.25-, 0.7-, and 1.5-m depth, respectively. In contrast, the Noah heat capacities were previously calculated from the sum of fractional contributions of prognostic liquid water content, prognostic total water substance, soil type and air (Chen and Dudhia 2001). Typical previous values for Greenland were about 2×10^6 J m^{-3}K^{-1}, about twice the new values. The thermal conductivities for the three lowest Noah layers are reduced by about a factor of 5 and set at 0.345, 0.399, and 0.473 W m^{-1}K^{-1}. These changes implement the strong thermal insulation for the upper firn over Greenland and reduce the ground heat flux.

4. Greenland domain and data

A crucial step in the development of Polar MM5 occurred during the late 1990s when an early version of the model was evaluated against 1997 observations during the Katabatic wind and boundary layer front experiment around Greenland (KABEG) study and against the Norwegian Limited Area Model (NORLAM) run at Meteorologisches Institut der Universität Bonn (Bromwich et al. 2001; Klein et al. 2001). Many of the polar optimizations to MM5 were included during the course of that work. Thus, it is natural we evaluate WRF for a similar domain. It is anticipated that Polar WRF will replace Polar MM5 in numerical studies assisting in the calculation of the Greenland ice budget (e.g., Box et al. 2006). The relevance is emphasized by new studies demonstrating rapid changes in the Greenland hydrology (e.g., Velicogna and Wahr 2006).

After initially experimenting with the extensive North Atlantic grid with 40-km resolution used by Bromwich et al. (2001), we selected a smaller area, but higher-resolution 24-km grid used for continuing Greenland and Iceland studies with Polar MM5 following Bromwich et al. (2005a). The grid is a polar stereo-

graphic projection centered at 71°N, 30°W consisting of 97 points in the east–west direction and 139 points in the north–south direction (Fig. 1). The 24-km resolution well captures the surface topography for a large majority of the Greenland surface area, particularly where the permanent ice is hundreds or thousands of meters thick.

For validation, automatic weather station (AWS) data are readily available from the Program for Arctic Regional Climate Assessment (PARCA) Greenland Climate Network (GC-Net; Steffen and Box 2001; Box et al. 2004). Sixteen AWS sites produced usable data for this study, including stations on the high interior and along the sloping ice sheet flanks (Table 1, Fig. 1). Box and Rinke (2003) estimate an uncertainty of 1 K for the monthly-mean AWS 2-m temperature, while the uncertainty in wind speed is about 0.1 m s^{-1}. For accurate katabatic wind simulations, the Greenland topography is adapted from the high-resolution Ekholm (1996) digital elevation data to best capture the interior heights and steep escarpment of the ice sheet. For the Greenland portion of the domain, mass point grid locations and surface elevation are identical to those of Bromwich et al. (2005a). The 24-km horizontal grid spacing adequately resolves the terrain slopes over all but the steepest margins of the ice sheet. Additionally, shortwave and longwave radiation measurements at Summit (72.5794°N, 38.5042°W, 3208 m ASL) are available for June 2000–June 2002. Surface energy flux estimates for sensible heat, latent heat, and ground heat flux are available for 2001–02 at the Greenland Summit Environmental Observatory operated by the Swiss Federal Institute for Environmental Research and Technology (ETH; Ohmura 2001; Bourgeois et al. 2006).

A summer month, June 2001, and a winter month, December 2002, with extensive AWS observations are simulated with a series of 48-h integrations, each initialized at 0000 UTC. The initial subsurface temperature over Greenland was vertically interpolated from the initial conditions of the previous Polar MM5 simulations over the same domain. These values were found to be resistant to large temperature drift during the WRF simulations. For the spinup in the atmosphere, Parish and Waight (1987) examined boundary layer development in an idealized mesoscale simulation of the katabatic wind over an ice sheet. They showed large adjustments to the boundary layer fields before the fields began to stabilize after about 10 h. In subsequent studies, Bromwich et al. (2001) took the first 24 h as an adjustment period for Polar MM5 to spin up the Greenland boundary layer and the hydrologic cycle. Later, Bromwich et al. (2005a) used a 12-h spinup. For the current WRF simulations, we find there is very little

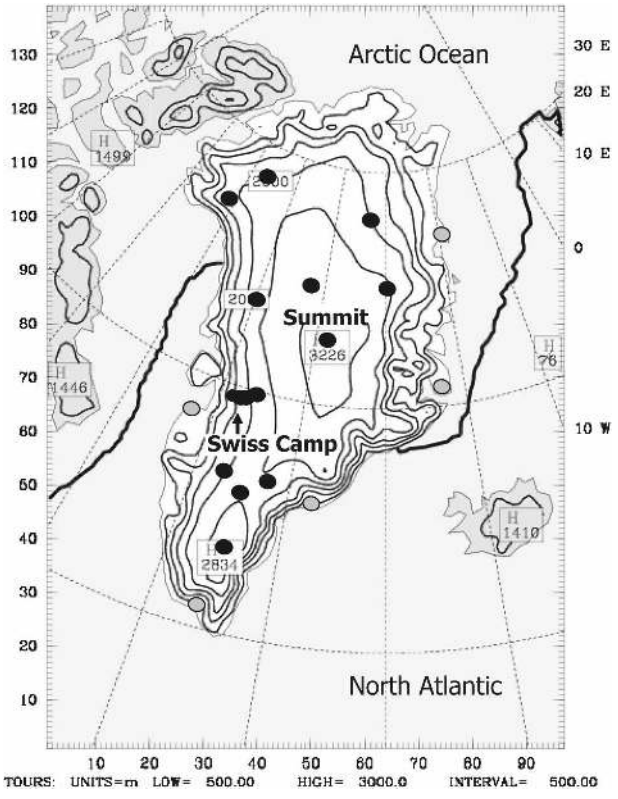

FIG. 1. Map of Polar WRF model domain with terrain elevation contours at 500-m intervals. Thick line shows average southern boundary of sea ice for December 2002. Solid circles show locations of AWS. Gray circles show locations of rawinsondes.

difference between 12- and 24-h spinup times when comparing model results to atmospheric results. Therefore, a 12-h spinup is selected for convenience in comparison to Bromwich et al.'s (2005a) results. Thus, the first 12 h are then discarded, and the 12–33-h forecasts (one forecast for each day) are combined into a month-long output field at 3-h intervals.

Previous 30-h Polar MM5 simulations of December 2002 and June 2001 by Bromwich et al. (2005a) are compared with the Polar WRF simulations. These Polar MM5 simulations are performed on a 24-km horizontal resolution grid nested inside the larger 72-km resolution domain (see Fig. 1 of Bromwich et al. 2005a). The inner grid consisted of 121 × 103 grid points and was shifted slightly east toward Iceland compared to the grid in Fig. 1. In the vertical, 28 levels are located at heights approximately similar to those for Polar WRF. Seven levels are within the lowest 400 m with the lowest about 12 m AGL, and the top is similarly located at 10 hPa. A higher-resolution grid over Iceland is not considered for the present study. Large-scale cloud and precipitation processes for Polar MM5 are represented by the Reisner scheme, with the Grell cumulus scheme

TABLE 1. List of GC-Net AWS for model verification during June 2001 and December 2002. Available AWS observations include P (surface pressure), T (2-m temperature), Q (2-m specific humidity), S (10-m wind speed), and D (10-m wind direction). Asterisks indicate data are available from JAR2 and JAR3 but are not included in statistics for Tables 2 and 4.

Station	Lat (°N)	Lon (°W)	Elev (m)	Available observations	
				Dec 2002	Jun 2001
Swiss Camp	69.5732	49.2952	1149	P, T, Q, S, D	P, T, Q, S, D
Crawford Point	69.8819	46.9736	2022	T, Q, S, D	T, Q, S, D
NASA-U	73.8333	49.4953	2368		T, S, D
GITS	72.1433	61.0950	1887		T, Q, S, D
Humboldt Glacier	78.5266	56.8305	1995	P, T, S, D	P, T, Q, S, D
Summit	72.5794	38.5042	3208	P, T, Q, S, D	P, T, Q, S, D
Tunu-N	78.0168	33.9939	2020	P, T, Q, S, D	P, T, S, D
DYE-2	66.4810	46.2800	2165	T, Q, S, D	
JAR1	69.4984	49.6816	962	P, T, Q, S, D	P, T, Q, S, D
Saddle	66.0006	44.5014	2559	S, D	T, Q, S, D
South Dome	63.1489	44.8167	2922	P, T, Q, S, D	P, T, Q, S
NASA-E	75.0000	29.9997	2631	P, T, Q, S, D	
NGRIP	75.0998	42.3326	2950	P, T, Q, S, D	P, T, Q, S, D
NASA-SE	66.4797	42.5002	2579	T, Q, S, D	T, Q, S, D
JAR2	69.4200	50.0575	568	P, T, Q, S, D*	P, T, Q, S, D*
JAR3	69.3954	50.3104	323	P, T, Q, S, D*	P, T, Q, S, D*

for subgrid-scale convection. Radiation is calculated with the Community Climate Model, version 2, (CCM2) scheme. Polar MM5 simulations are initialized at 0000 UTC with the lateral boundaries updated twice daily from 2.5° × 2.5° operational analyses of the European Centre for Medium-Range Weather Forecasts (ECMWF).

5. December 2002 simulations

The evaluation of WRF begins with the winter month December 2002 when little solar radiation falls on Greenland, and most of that reaching the surface is reflected. Thus, the diurnal cycle tends to be weak. Simulated meteorological fields over Greenland will primarily be driven by (i) stable boundary layer processes over the ice sheet surface, including sensible heat exchange between the atmosphere and ice sheet; (ii) longwave radiation, expected to provide a strong cooling at the ice sheet surface; and (iii) North Atlantic synoptic forcing.

First, we evaluate the WRF physics options including the YSU and MYJ PBL schemes, the Noah and RUC land surface models, and the one-moment WSM5 and two-moment Thompson et al. (2004) cloud microphysics. The so-called base run, performed first with Polar WRF, is taken as the simulation with the YSU PBL, the Noah LSM, and the Thompson et al. microphysics. The average 500-hPa geopotential height and sea level pressure during December 2002 for the base run are shown in Fig. 2. The sea level pressure field reveals a negative North Atlantic Oscillation (NAO) pattern with above average pressure near Iceland (Fig. 2b). The normalized NAO Index for this month is −2.4 hPa according to the Web site of J. Hurrell (http://www.cgd.ucar.edu/cas/jhurrell/indices.data.html#naostatmon). A 994-hPa low at the surface is located south of Greenland, and southeasterly flow over the North Atlantic approaches the southeastern coast of Greenland, with a narrow ridge near the coastline. At 500 hPa, Greenland is located in south-southwesterly geostrophic flow between a trough offshore from Labrador and a ridge over the Norwegian Sea (Fig. 2a). This flow pattern produced relatively heavy snowfall (not shown) over southeastern Greenland.

Simulations are also performed replacing a component of the base run configuration with one of the following optional components: (i) the WSM5 microphysics, (ii) the MYJ PBL, (iii) the RUC LSM, or (iv) both the WSM5 microphysics and the MYJ PBL. Model output is obtained horizontally at AWS sites through bilinear interpolation from the nearest four grid points. Velocity components are vertically interpolated to 10 m inside the WRF surface layer routines, and temperature is similarly interpolated to 2 m. The majority of model interpolated surface heights are within 100 m of the actual AWS elevations. Nevertheless, model 2-m temperature is adjusted to station height according to the annual average 0.0071 K m^{-1} decrease of surface temperature with height found by Steffen and Box (2001). Figure 3 shows the observed 2-m temperature and the interpolated values for the five WRF simulations every 3 h at Swiss Camp, a well-maintained observing site also

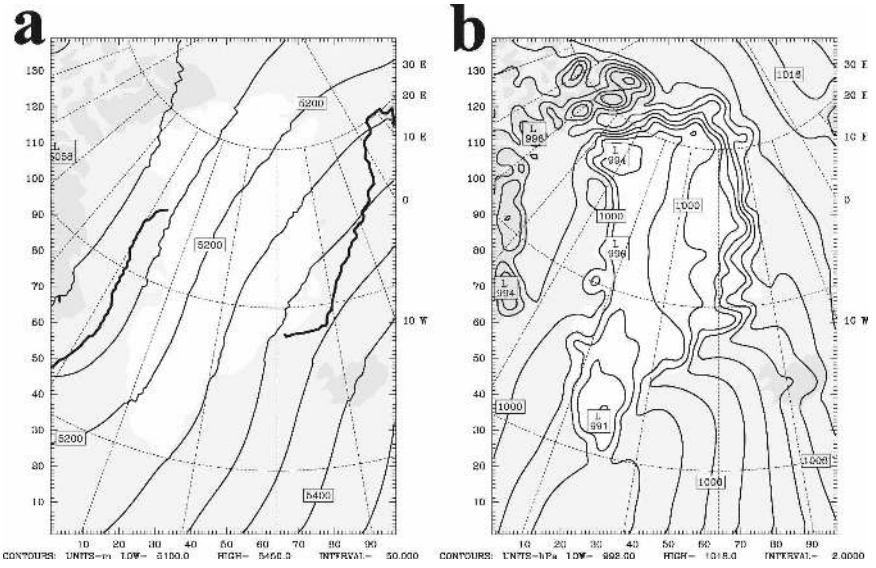

FIG. 2. Monthly average (a) 500-hPa geopotential height (m) and (b) sea level pressure (hPa) during December 2002 for the Polar WRF simulation. Contour interval is 50 m for (a) and 2 hPa for (b).

known as ETH/CU (CU denotes University of Colorado) (69.5732°N, 49.2952°W, 1149 m ASL) near the ice equilibrium line on the western slope of the Greenland ice sheet.

The configuration of WRF with the WRF single-moment microphysics, the MYJ PBL and the Noah LSM has the smallest magnitude bias, −0.1°C, while the WRF single-moment and RUC simulations have the highest correlation, 0.93. In general the performances of the WRF configurations are quite similar, and the differences are small. The WRF single-moment and MYJ simulation is coldest, and the other simulations show a warm bias. In comparison, Polar MM5 has a similar correlation, 0.93, at Swiss Camp; however, the cold bias of 2.6°C has a larger magnitude than the Polar WRF biases. Forecast error statistics for December 2002 were calculated in comparison to the available AWS data according to Table 1. The statistics, including correlation of the time variations, bias, and root-mean-square error (rmse) versus each individual station observation at 6-h intervals, were then averaged over the available sites with good observational data, except for Jakobshavn Ablation Region sites 2 and 3 (JAR2 and JAR3), which are very close to Swiss Camp.

Table 2 shows the average of the statistics computed at individual sites: 8, 11, 10, and 12 stations listed on Table 1 contribute to the averages for height-adjusted surface pressure, 2-m temperature, 2-m specific humidity, and 10-m wind speed, respectively. Model surface pressure is adjusted hydrostatically to AWS station heights using the model's second-lowest atmospheric level temperature and assuming a lapse rate of 0.005 K m^{-1}. Work with the Student's t test indicates that biases at an individual station of about 0.3°C for temperature and 0.3 m s^{-1} for wind speed are statistically significant at the 95% confidence level. As demonstrated by the Swiss Camp example shown in Fig. 3, the overall error statistics are similar for the five configurations of WRF. Table 2 indicates WRF with the WSM5 microphysics and the MYJ PBL has the lowest bias and rmse for 2-m temperature, and its performance is competitive for other variables. In comparison to the Polar MM5 simulation, WRF shows very similar winter correlations for the pressure, temperature, humidity, and wind speed. Polar MM5 has a relatively large magnitude bias, -0.29×10^{-3}, in 2-m specific humidity that is probably related to the cold bias. Polar MM5 also has a positive wind speed bias, 3.3 m s^{-1}, at 10 m. The speed bias for WRF tends to be roughly half as large. Polar MM5's small surface roughness, 10^{-4} m, contributes to the difference. In contrast, the RUC LSM uses 0.05 m over the Greenland ice sheet and shows a negative wind speed bias of 1.0 m s^{-1}. The simulations with the Noah LSM assign a surface roughness of 10^{-3} m and have intermediate speeds at 10 m. The 9.8 m s^{-1} average speed shown in Table 2 for the MYJ PBL simulation is exaggerated due a correction of model velocity to 10 m inside the MYJ scheme that is inconsistent with the surface roughness set in the Noah LSM. Fortunately, this error impacts only the model output, not the internal physics of the MYJ scheme. The interpolation to 10 m was corrected for the simulation with both the

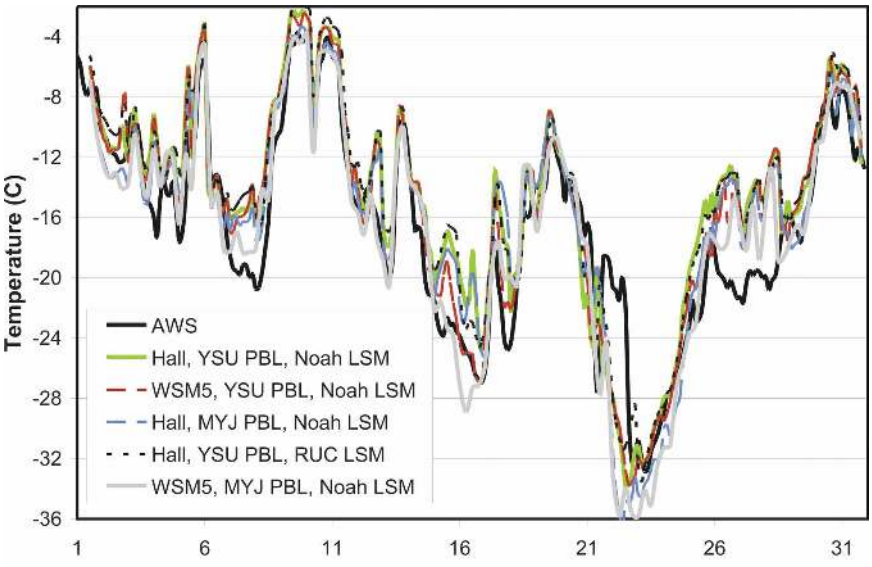

Run	Correlation	Bias	RMSE
Hall, YSU PBL, Noah LSM	0.92	1.4	3.1
WSM5, YSU PBL, Noah LSM	0.93	1.0	2.8
Hall, MYJ PBL, Noah LSM	0.91	0.4	3.0
Hall, YSU PBL, RUC LSM	0.93	1.6	3.1
WSM5, MYJ PBL, Noah LSM	0.92	-0.1	3.1
Polar MM5	0.93	-2.6	3.7

FIG. 3. Temperature (°C) at 2-m AGL for Swiss Camp, Greenland (69.5732°N, 49.2952°W, 1149 m ASL) every 3 h during December 2002 for AWS observations and WRF simulations. The WRF simulations have the Goddard shortwave and RRTM longwave radiation schemes. Model performance statistics for WRF and MM5 are shown.

WSM5 microphysics and the MYJ PBL resulting in a reduced 10-m speed, 9.2 m s^{-1}, that is closer to the observed average value 7.7 m s^{-1}.

Figure 4 displays observed and modeled 10-m wind speed for Swiss Camp, where strong katabatic winds are expected during winter. The figure shows speed at 3-h intervals, although the statistics shown below the figure, including those for Polar MM5, are calculated with 6-h intervals. Consistent with average behavior noted in Table 2, the RUC LSM simulation tends to undersimulate wind speed at Swiss Camp by an average of 2.6 m s^{-1}. In contrast, the simulations with the Noah LSM tend to oversimulate speed, but have smaller RMSE. Based on the results shown in Figs. 3 and 4, along with results at other sites (not shown), and the average AWS statistics from Table 2, we select the WRF configuration with the WSM5 microphysics, the Noah LSM and the MYJ PBL for further analysis for the remainder of this paper. We now concentrate on comparing the results of Polar WRF with those of Polar MM5 over the Greenland domain.

Figure 5 shows the December 2002 surface pressure, adjusted to AWS station height for Swiss Camp and Summit. The high-altitude site atop the Greenland ice sheet is also well maintained, is near the Greenland Ice Core Project (GRIP) and Greenland Ice Sheet Project (GISP) ice core sites, and is used for ongoing meteorological studies. Both Polar WRF and Polar MM5 well capture the pressure variations with time, with correlations of 0.98 or greater. Adjusted surface pressure tends to be slightly higher for WRF than for MM5. The correlations for 2-m temperature are not as high as for surface pressure, yet they are still quite large (Fig. 6). Furthermore, a systematic cold bias for Polar MM5, −2.6° at Swiss Camp and −2.3° at Summit, is replaced by a bias of −0.1° at Swiss Camp and a warm bias of 3.0° at Summit for Polar WRF. The differences can be attributed to the radiation budget as Polar MM5 has a known deficit in downward longwave flux (Guo et al. 2003). Radiation measurements were not available for December 2002; however, values are available at Summit for December 2000 and December 2001. The incident longwave radiation at the surface for Polar WRF, is 162.9 W m^{-2}, which is between the observed values for 2000 (139.9 W m^{-2}) and 2001 (164.8 W m^{-2}). In contrast, incident longwave radiation (109.7 W m^{-2}) is much smaller for Polar MM5. Thus, the magnitude of MM5's net radiation, 43.6 W m^{-2}, is almost twice as

TABLE 2. Performance statistics of Polar WRF and Polar MM5 during December 2002 for short-term forecasts compared with Greenland observations from GC-Net AWS sites. Numbers shown are the averages of the statistics calculated individually for multiple sites from Table 1 not including JAR2 and JAR3. Polar MM5 and Polar WRF output includes 12-, 18-, 24-, and 30-h forecasts. The range of error statistics for the WRF simulation with the WSM5 microphysics and the MYJ PBL is displayed below the means with minimum (italics) and maximum (boldface) values at AWS sites. Underlining highlights values with lowest magnitude bias and rmse and highest correlation (corr).

Variable	Simulation	Mean	Bias	Corr	Rmse
Surface pressure (hPa)	Polar MM5	755.1	−0.9	0.97	3.2
	WRF Base	754.5	−1.5	0.98	3.5
	WRF with WSM5	754.6	−1.4	0.98	3.5
	WRF with MYJ PBL	755.5	−1.5	0.98	3.5
	WRF with RUC LSM	754.4	−1.5	0.98	3.5
	WRF WSM5 + MYJ	754.6	−1.4	0.98	3.4
			−6.8, **3.3**	*0.96*, **0.99**	*1.0*, **7.0**
2-m temperature (°C)	Polar MM5	−29.4	−2.3	0.89	4.7
	WRF Base	−23.6	3.5	0.91	5.1
	WRF with WSM5	−24.3	2.8	0.91	4.7
	WRF with MYJ PBL	−25.0	2.1	0.90	4.5
	WRF with RUC LSM	−23.3	3.8	0.90	5.4
	WRF WSM5 + MYJ	−25.9	1.2	0.90	4.1
			−1.2, **3.0**	*0.80*, **0.94**	*3.1*, **6.0**
2-m specific humidity (10^{-3})	Polar MM5	0.45	−0.29	0.85	0.43
	WRF Base	0.82	0.08	0.87	0.32
	WRF with WSM5	0.78	0.04	0.87	0.31
	WRF with MYJ PBL	0.74	0.01	0.88	0.30
	WRF with RUC LSM	0.77	0.04	0.88	0.29
	WRF WSM5 + MYJ	0.69	−0.05	0.87	0.29
			−0.61, **0.21**	*0.74*, **0.93**	*0.17*, **0.87**
10-m wind speed (m s^{-1})	Polar MM5	11.0	3.3	0.81	4.4
	WRF Base	9.2	1.5	0.81	3.1
	WRF with WSM5	9.4	1.7	0.81	3.2
	WRF with MYJ PBL	9.8	2.1	0.81	3.4
	WRF with RUC LSM	6.6	−1.0	0.81	2.9
	WRF WSM5 + MYJ	9.2	1.6	0.82	2.9
			−0.2, **3.4**	*0.65*, **0.95**	*1.7*, **4.2**

large as the Polar WRF value, 23.2 W m^{-2} (for other configurations of WRF, net radiation varied between 17.4 and 25.8 W m^{-2}). The excessive longwave cooling for Polar MM5 must be approximately balanced by sensible heat from the atmosphere to the surface. Thus, MM5's sensible heat flux magnitude, 37.1 W m^{-2}, is much larger than WRF's value, 22.7 W m^{-2}. The average flux of heat *from* the surface to the substrate, 0.8 W m^{-2} for WRF, appears to be reasonable.

Vertical profiles of atmospheric temperature at locations over Greenland are displayed in Fig. 7. For comparison with the model results, rawinsonde observations of monthly average temperature, geopotential, and velocity components at standard levels were obtained from the Integrated Global Rawinsonde Archive (Durre et al. 2006). Profiles are available from 5 coastal Greenland stations: Egedesminde (68.70°N, 52.85°W), Narssarssuaq (61.18°N, 45.42°W), Danmarkshavn (76.77°N, 18.77°W), Scoresbysund (70.48°N, 21.95°W), and Ammassalik (65.60°N, 37.63°W) for December 2002. For convenience, we will only show results for profiles at Egedesminde on the western coast of Greenland close to Swiss Camp site, at Scoresbysund on the eastern coast and at roughly similar latitude as Summit, and Ammassalik. Standard level temperatures are supplemented by hydrostatically computed temperatures at intermediate levels. Boxes show observed data points in Fig. 7. Unlike the AWS sites, the rawinsonde sites are heavily influenced by complex local terrain at the coastal locations. Therefore, caution should be applied in comparing simulated profiles to observed profiles in the lower troposphere. The Fig. 7 profile is colder at Egedesminde than Scoresbysund indicating an eastward component to the temperature gradient. Very good agreement between simulations and the observations is seen in the middle and upper troposphere, where the profiles are heavily influenced by large-scale processes. Both profiles, however, show a slight warm bias at 600 hPa. Some differences between the stations are also apparent at the tropopause and in the lower stratosphere. As mid- and upper-tropospheric features, such as those displayed in Fig. 7, are more readily cap-

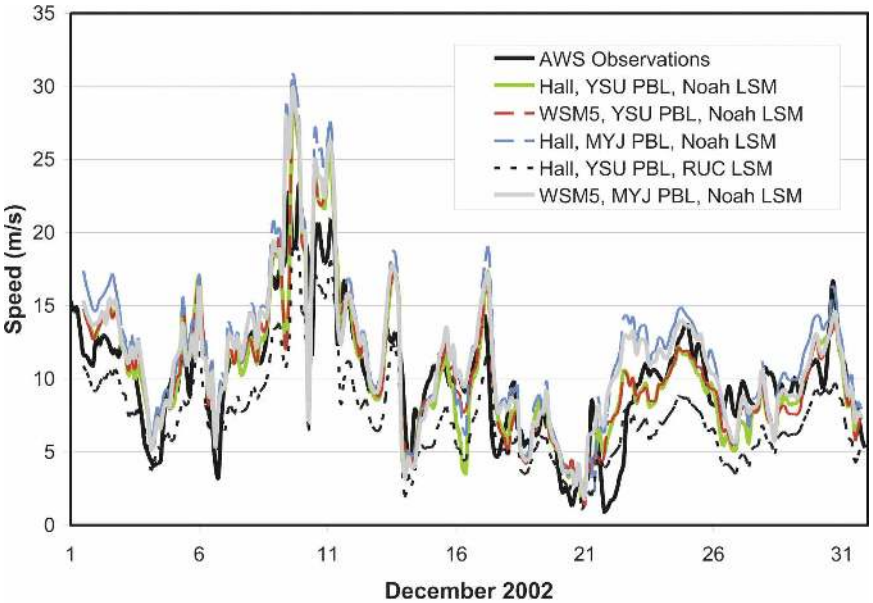

Run	Correlation	Bias	RMSE
Hall, YSU, Noah	0.83	0.3	2.6
WSM5, YSU, Noah	0.84	0.4	2.5
Hall, MYJ, Noah	0.84	1.9*	3.3
Hall, YSU, RUC	0.84	-2.6	3.4
WSM5, MYJ, Noah	0.85	1.2	2.8
Polar MM5	0.75	4.4	5.5

FIG. 4. As in Fig. 3, but for wind speed (m s^{-1}) at 10 m AGL.

tured, we should prioritize simulating the surface and boundary layer effects within mesoscale modeling studies of Greenland climate.

Figure 8 shows the 10-m wind speed for Summit and Swiss Camp. Wind speed for Swiss Camp (Summit) corresponds to the scale on the left (right). Wind speed is typically higher along the western Greenland slopes at Swiss Camp because of the katabatic drainage, while the value at Summit in central Greenland is largely driven by synoptic events (e.g., Stearns et al. 1997). The December wind speed at Swiss Camp is clearly better simulated by Polar WRF than by Polar MM5. The former has a correlation of 0.85 and a bias of 1.2 m s^{-1}, while the latter has values of 0.75 and 4.4 m s^{-1}, respectively. In contrast, Polar MM5 has a slightly higher correlation at Summit, 0.87, than that for Polar WRF, 0.85. A positive wind speed bias is again seen for Polar MM5 with an excess of 2.5 m s^{-1}. The bias is smaller, 1.5 m s^{-1}, for Polar WRF. Both Polar MM5 and Polar WRF very well capture the time variation of wind direction (not shown).

Figure 9 shows vertical profiles of the modeled and observed vector-average speed and direction during December 2002. The southeastern Greenland station Ammassalik, not shown in Fig. 7, is included along with Egedesminde and Scoresbysund. The observed simulated resultant wind speed profiles show a similar pattern over most of the depth of the troposphere with the speed between 6–8 m s^{-1} at 700 hPa and steadily increasing to 14–22 m s^{-1} near the tropopause (Fig. 9a). Similar behavior is seen with the Polar WRF profiles. Resultant wind direction is more scattered in the lower troposphere where local topographical channeling is important and converges toward southwesterly near the tropopause (Fig. 9b). At Scoresbysund, the observed lower-tropospheric wind drains off the ice sheet to the west, while the simulated direction is from the south-southwest and more parallel to the model's topography shown in Fig. 1. At higher levels, both observations and the simulation show the southwesterly flow at Scoresbysund (Fig. 2). The simulation also displays the observed wind direction shift with height at Egedesminde and Ammassalik.

In summary, the Polar WRF simulation appears to be at least as skillful as Polar MM5 in simulating the near-surface temperature and wind speed for the highly stable winter boundary layer. Furthermore, Fig. 10 shows that Polar WRF has similar correlations to the observations as Polar MM5 and with much smaller biases and RMSE for the specific humidity at 2 m AGL. The negative humidity bias for Polar MM5 can be attributed to the model's representation of longwave ra-

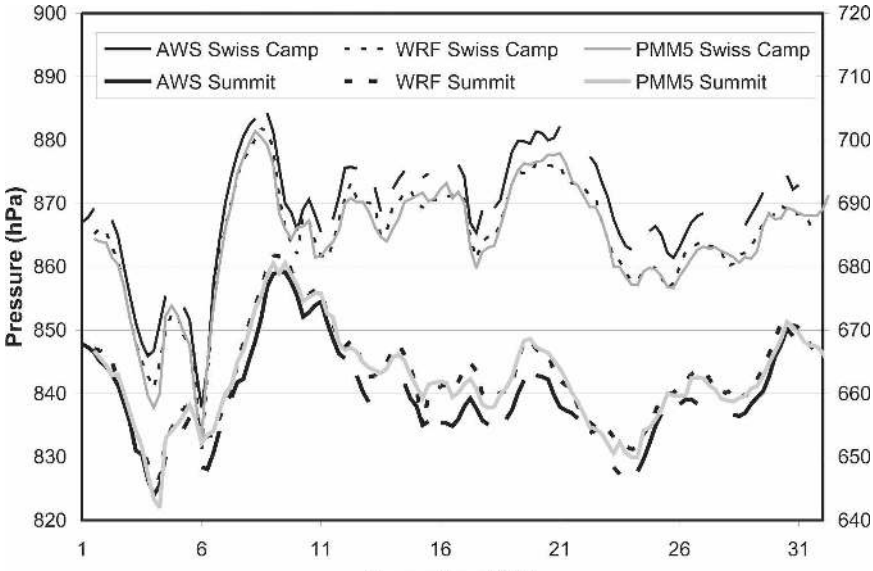

Run	Correlation	Bias	RMSE
Polar WRF - Swiss Camp	0.99	-4.2	4.4
Polar MM5 – Swiss Camp	0.99	-4.6	4.9
Polar WRF - Summit	0.98	3.3	3.6
Polar MM5 – Summit	0.98	2.8	3.4

FIG. 5. Adjusted surface pressure (hPa) for Swiss Camp (left scale) and Summit (72.5794°N, 38.5042°W, 3208 m MSL, right scale) stations every 6 h during December 2002 for AWS observations and Polar MM5 and Polar WRF simulations. The WRF simulations have the WRF single-moment 5-class microphysics, the MYJ PBL, and the Noah LSM.

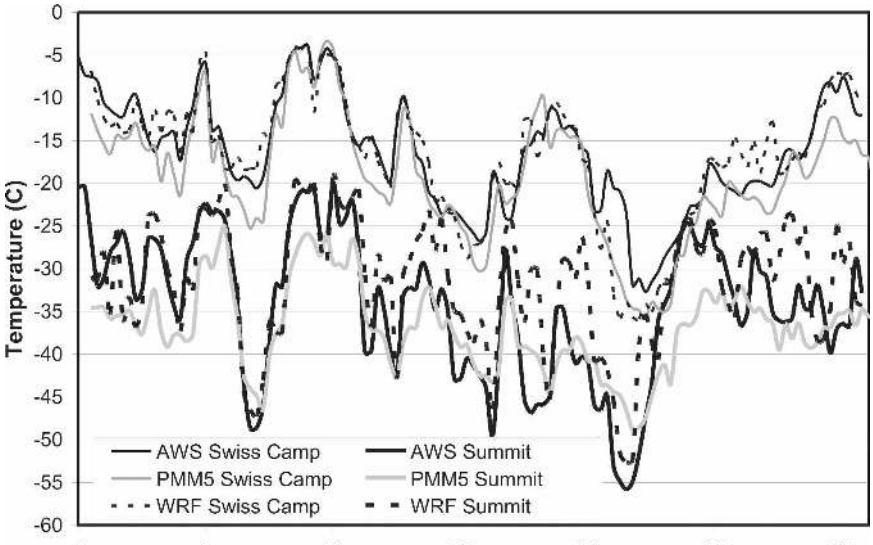

Run	Correlation	Bias	RMSE
Polar WRF - Swiss Camp	0.92	-0.1	3.1
Polar MM5 – Swiss Camp	0.93	-2.6	3.7
Polar WRF - Summit	0.80	3.0	6.0
Polar MM5 – Summit	0.84	-2.3	5.6

FIG. 6. As in Fig. 5, but for temperature (°C) at 2 m AGL.

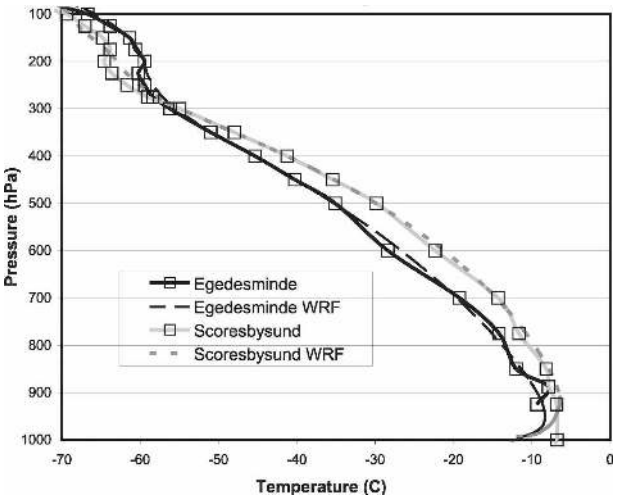

FIG. 7. Average temperature profiles for Egedesminde and Scoresbysund during December 2002 from observations (solid lines) and WRF simulations (dashed lines). Boxes show data points for the observations.

diation, leading to a colder, drier surface layer. In the next section, June 2001 observations of shortwave and longwave radiation allow us to examine their representation by both Polar MM5 and Polar WRF.

6. June 2001 simulation

The simulation of June 2001 will be strongly influenced by shortwave radiation, which will drive a diurnal cycle due to the variation of sun elevation. Preliminary work indicated that Goddard shortwave schemes best represent the diurnal cycle of solar radiation reaching the Greenland surface, so all of the Polar WRF simulations shown here include that scheme. The Polar WRF simulation for June 2001 employs the Noah LSM, the MYJ PBL, and the WSM5 microphysics. Comparisons are made to the Polar MM5 simulation of this month and to radiation measurements at Summit.

The diurnal cycle of incident longwave radiation versus local standard time (LST) at Summit is displayed in Fig. 11. Data are plotted every 3 h for the observations and WRF and every 6 h for Polar MM5. Figure 11 shows monthly minima, maxima, and averages. The diurnal cycle of observed longwave radiation is small. The average hourly downward longwave generally stays within 5% of the mean value, 191.3 W m^{-2}. A simple way to define a realistic range for the month is the hourly minimum and maximum values shown in Fig. 11. The minimum can be taken to represent clear-sky conditions, while the maximum will be heavily influenced by clouds. The large change for the Polar MM5 maximum between 0900 and 1500 LST suggest that the model has not fully spun up the atmospheric clouds by hour 12 of the forecast (0900 LST). The Polar WRF simulation with the Goddard shortwave scheme and the RRTM longwave scheme well captures the range and the average value of *longwave* radiation, with

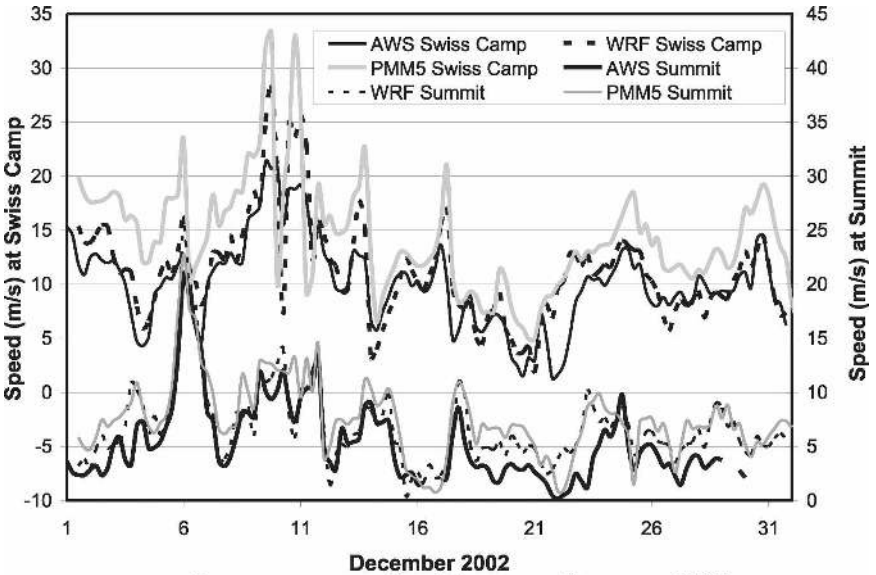

Run	Correlation	Bias	RMSE
Polar WRF - Swiss Camp	0.85	1.2	2.8
Polar MM5 – Swiss Camp	0.75	4.4	5.5
Polar WRF - Summit	0.85	1.5	2.4
Polar MM5 – Summit	0.87	2.5	3.1

FIG. 8. As in Fig. 5, but for wind speed (m s^{-1}) at 10 m AGL.

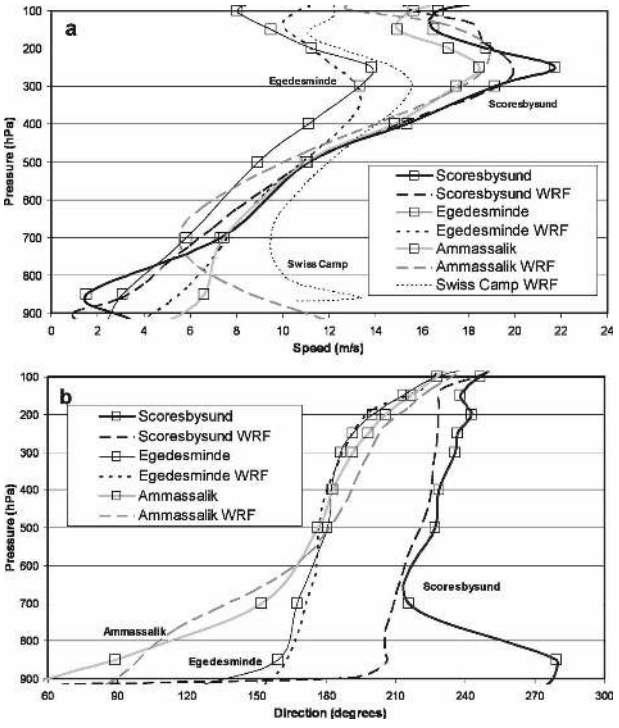

FIG. 9. Vertical profiles for Scoresbysund, Egedesminde, and Ammassalik during December 2002 from observations (solid lines) and WRF (dashed/dotted lines) showing (a) speed (m s^{-1}) and (b) direction (°) of the monthly average velocity.

an average bias of only 3.5 W m^{-2}. On the other hand, Polar MM5 shows a significant deficit for the average diurnal cycle (Fig. 11). The deficit is especially large, 68.8 W m^{-2}, for maximum downward longwave radiation at 0900 LST, which can be attributed to insufficient downwelling radiation from cloud bases in the Polar MM5 simulation (e.g., Guo et al. 2003).

Diurnal cycles for incident shortwave radiation at Summit during June 2001 are displayed in Fig. 12. Shortwave radiation, unlike longwave radiation, has a large diurnal cycle. The curves for Polar MM5 appear somewhat smoother because of the less frequent sampling. Interestingly, Polar MM5 replicates a smoothed representation of the diurnal cycle seen for observed shortwave radiation, although the simulated longwave radiation does not match the observed diurnal cycle in Fig. 11. The Polar WRF simulates an average daily incident shortwave radiation of 409.8 W m^{-2} as compared with the observed value 392.8 W m^{-2}. The largest bias occurs during morning hours at Summit, when the excess reaches 64.7 W m^{-2} at 0600 LST. The simulated net shortwave radiation 82.0 W m^{-2} is also larger than the observed 72.2 W m^{-2} and the Polar MM5 value 79.5 W m^{-2}. An increase of the albedo from 0.80 to the observed value of 0.82 at Summit would remove most of the net bias. The June 2001 surface energy balance statistics at Summit for the observations, Polar MM5,

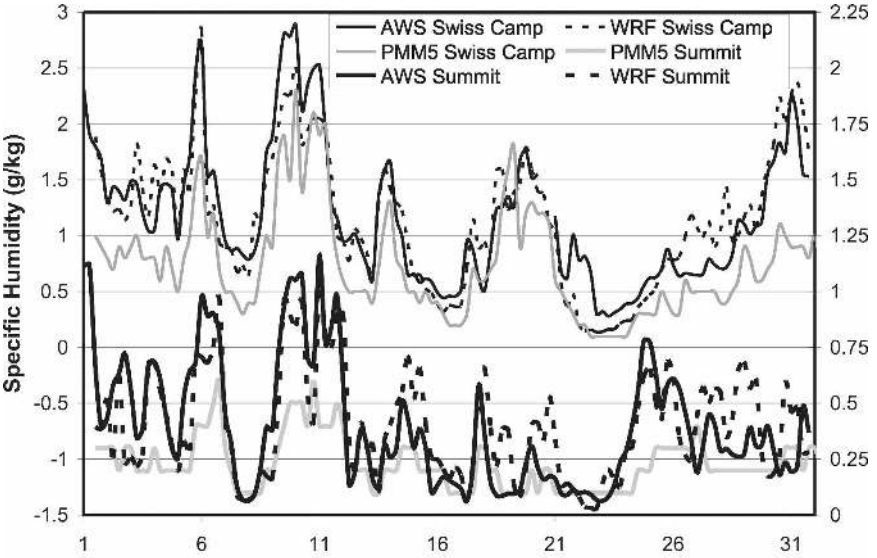

Run	Correlation	Bias	RMSE
Polar WRF - Swiss Camp	0.90	-0.01	0.27
Polar MM5 – Swiss Camp	0.89	-0.38	0.69
Polar WRF - Summit	0.74	0.03	0.18
Polar MM5 – Summit	0.77	-0.14	0.23

FIG. 10. As in Fig. 5, but for specific humidity (10^{-3}) at 2 m AGL.

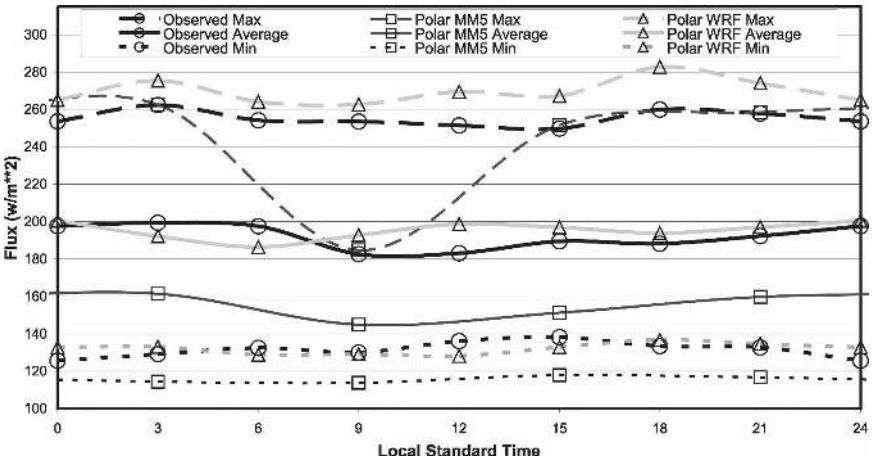

FIG. 11. Diurnal cycle of incident longwave radiation (W m^{-2}) at Summit showing hourly average, minimum, and maximum values during June 2001 for observations (every 3 h) and Polar MM5 (every 6 h) and Polar WRF simulations (every 3 h). The WRF simulation has the MYJ PBL, the Noah LSM, WSM5 microphysics, and the Goddard shortwave scheme.

and Polar WRF simulations are displayed in Table 3 with a sign convention consistent with Eq. (1).

Similar to Fig. 11, Table 3 demonstrates the large difference between Polar MM5 and Polar WRF in simulating the longwave radiation. Particularly striking is the large magnitude MM5 bias for incident longwave radiation, -37.0 W m^{-2}, in comparison with 3.5 W m^{-2} for WRF. Ground heat flux for Summit was not available for June 2001; however, a representative monthly value of -9.0 W m^{-2} from June 2002 is shown in Table 3. The apparent WRF bias of 6.8 W m^{-2} is plausibly within the range of interannual variability. The larger magnitude of latent heat flux, 4.3 W m^{-2} for WRF as compared with 0.6 W m^{-2} for MM5, may be related to the Penman–Monteith formula for the former and the classic bulk aerodynamic treatment for the latter. Results of June simulations (not shown) with the Thompson et al. (2004) microphysics suggest that excessive surface evaporation with the Penman–Monteith formula may saturate the boundary layer and induce spurious water clouds. Overall, the surface radiation balance for June 2001 appears to be better simulated with Polar WRF than with Polar MM5.

The June 2001 simulations were also evaluated by statistical comparison to AWS observations for June 2001. Table 4 shows the average of the model performance statistics for the AWS locations in Table 1. Up to 12 stations are available for the June 2001 average. The sites JAR2 and JAR3 are excluded in the average as in Table 2. Minimum and maximum values are added in

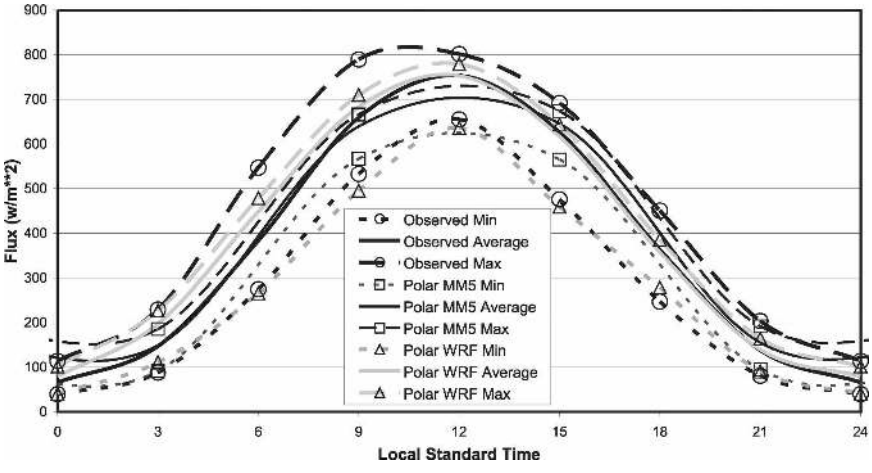

FIG. 12. As in Fig. 11, but for incident shortwave radiation.

TABLE 3. Observed and simulated surface energy balance statistics averaged over June 2001 at Summit (W m^{-2}). Net radiation with a positive sign implies a heat gain at the surface. Sensible heat flux, latent heat flux, and net longwave radiation are directed upward from the earth's surface to the atmosphere for positive values. Ground heat flux is directed upward from the subsurface to the surface (surface heat gain), and net shortwave radiation is directed downward from the atmosphere to the surface for positive values. Values in boldface show fluxes or flux biases contributing to surface warming. Observed values in parentheses are estimates for the following year (2002) from ETH.

Field	Obs value	Polar MM5 Bias	Polar WRF Bias
Shortwave down	**392.8**	**4.5**	**17.0**
Shortwave up	320.6	**−2.8**	7.2
Net shortwave (down)	**72.2**	**7.3**	**9.8**
Longwave down	**191.3**	−37.0	**3.5**
Longwave up	245.1	**−14.7**	9.0
Net longwave (up)	53.7	22.4	9.5
Net radiation (down)	**18.4**	−15.1	**0.4**
Sensible heat flux	0.0 (**−1.5**)	**−2.9**	12.3
Latent heat flux	2.5 (10.5)	**−1.9**	1.8
Ground heat flux	(−9.0)		**6.8**

italics and boldface, respectively, to demonstrate the range over the AWS locations. After a review of the observed data quality, the sites Crawford Point, NASA-U, Greenland Ice Sheet Training Facility (GITS), Saddle, and NASA-SE are not included in the average for pressure, and NASA-U and Tunu-N are not included for specific humidity. Table 4 shows that, overall, Polar WRF has similar, but slightly less forecast skill than Polar MM5 for June 2001. Polar WRF does show a larger average magnitude bias, −3.6 hPa for adjusted surface pressure bias than Polar MM5, −2.0 hPa. There is a small warm bias for WRF, whereas MM5 still has a cold bias. Interestingly, Polar MM5 does not show a systematic bias for 10-m wind speed during June 2001, unlike the December 2002 case. On the other hand, WRF now shows a slight negative bias, −0.9 m s^{-1}, for the speed.

Figure 13 shows the June 2001 2-m temperature values as a function of time for observations at Swiss Camp and Summit, the Polar MM5 simulation, and the Polar WRF simulation. Both models show good skill at Swiss Camp and the synoptic variability appears to be very well captured. The models are less successful at Summit. There, Polar MM5 is superior to Polar WRF, and the former shows a cold bias of only 0.1°C. The warm bias for Polar WRF, 2.6°C, is clearly apparent for Summit in Fig. 13 over the majority of days during June and may be related to the excess net shortwave radiation (Table 3).

Figure 14 shows the June 2001 wind speed at 10 m AGL. At Swiss Camp, the WRF simulation shows a smaller magnitude bias, −0.3 m s^{-1}, and correlation, 0.77, and a similar RMSE, 2.0 m s^{-1}, to the attributes simulated by Polar MM5, 1.0 m s^{-1}, 0.83, and 2.1 m s^{-1}, respectively. The case is reversed at Summit where Polar MM5 has the smaller magnitude bias and WRF has the higher correlation. The RSME are again similar, 1.5 m s^{-1} for Polar WRF and 1.6 m s^{-1} for Polar MM5. In summary, from Figs. 13 and 14 and Table 4, it appears that the overall forecast skills of MM5 and WRF are similar for the summertime surface layer over the inte-

TABLE 4. Performance statistics of Polar WRF and Polar MM5 during June 2001 for short-term forecasts compared with 6-h Greenland observations from GC-Net AWS sites. Underlined numbers show the averages of the statistics calculated individually for all available sites from Table 1, except JAR2 and JAR3. The range of values across the AWS sites is shown with minimum (italics) and maximum (boldface) values. Asterisks highlight values with lowest magnitude bias and rmse and highest correlation (corr).

Variable	Simulation	Mean	Bias	Corr	Rmse
Surface pressure (hPa)	Polar MM5	778.6	−2.0*	0.91*	3.2*
			−4.3, **1.2**	*0.57*, **0.99**	*0.9*, **4.4**
	Polar WRF	777.0	−3.6	0.91*	4.7
			−5.2, **−0.8**	*0.56*, **0.99**	*1.1*, **5.3**
2-m temperature (°C)	Polar MM5	−8.7	−0.3*	0.83*	2.6*
			−1.3, **0.6**	*0.79*, **0.89**	*1.7*, **3.8**
	Polar WRF	−7.8	0.6	0.81	3.0
			−0.6, **2.6**	*0.76*, **0.89**	*1.8*, **4.7**
2-m specific humidity (10^{-3})	Polar MM5	2.50	−0.19	0.77*	0.72*
			−2.39, **0.49**	*0.55*, **0.88**	*0.38*, **2.53**
	Polar WRF	2.72	0.03*	0.77*	0.76
			−2.11, **2.17**	*0.68*, **0.86**	*0.44*, **2.33**
10-m wind speed (m s^{-1})	Polar MM5	6.6	0.0*	0.78*	1.9*
			−0.9, **1.0**	*0.68*, **0.84**	*1.5*, **2.5**
	Polar WRF	5.7	−0.9	0.78*	2.1
			−2.1, **0.0**	*0.68*, **0.86**	*1.5*, **2.8**

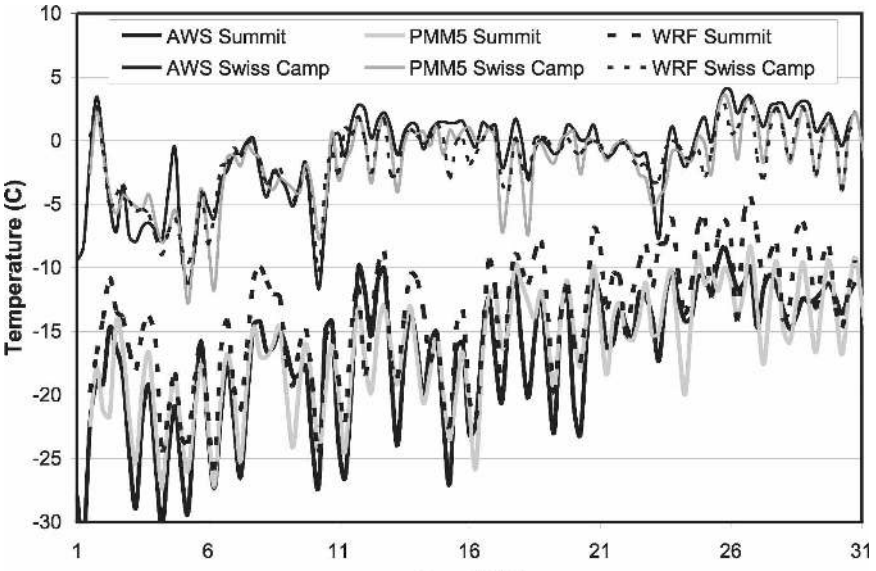

Run	Correlation	Bias	RMSE
Polar WRF - Swiss Camp	0.87	-0.6	1.8
Polar MM5 – Swiss Camp	0.86	-0.7	1.9
Polar WRF - Summit	0.76	2.6	4.8
Polar MM5 – Summit	0.79	-0.1	3.8

FIG. 13. Temperature (°C) at 2 m for Swiss Camp and Summit every 6 h during June 2001 for AWS observations and Polar MM5 and Polar WRF simulations.

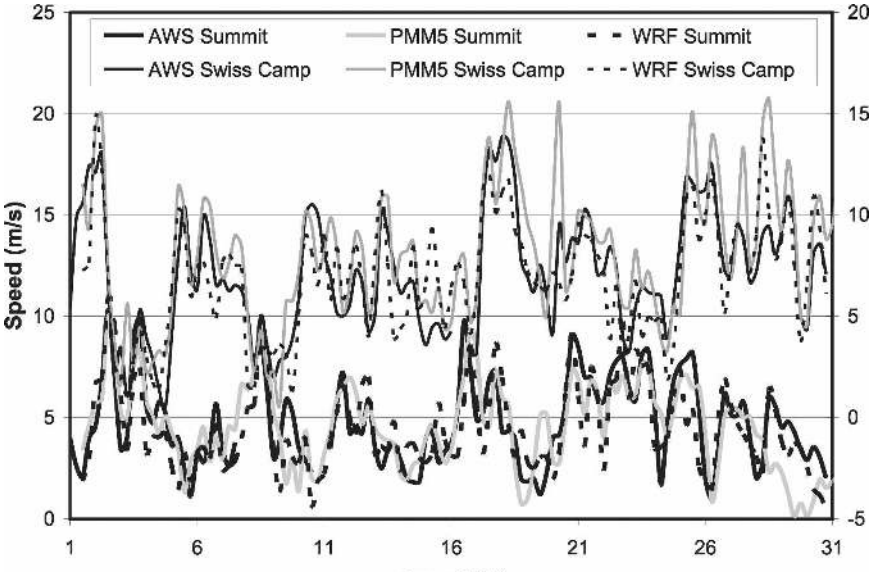

Run	Correlation	Bias	RMSE
Polar WRF - Swiss Camp	0.77	-0.3	2.0
Polar MM5 – Swiss Camp	0.83	1.0	2.1
Polar WRF - Summit	0.75	-0.3	1.5
Polar MM5 – Summit	0.72	-0.1	1.6

FIG. 14. As in Fig. 13, but for wind speed ($m\ s^{-1}$) at 10 m AGL.

rior Greenland Plateau and along the katabatic slopes at Swiss Camp in western Greenland.

7. Summary and conclusions

The development of Polar WRF is expected to provide an improved model for Arctic and Antarctic climate and synoptic applications. Following the path used to develop Polar MM5, testing begins with simulations of the Greenland ice sheet region. Previously, the polar-optimized MM5 achieved an improved performance through a careful series of tests in polar climates. Evaluations and optimizations for WRF are especially needed for the boundary layer parameterization, cloud physics, snow surface physics, and sea ice treatment. Therefore, a series of simulations based on WRF version 2.1.1 are performed with a 97×139 horizontal domain with 24-km resolution. The winter month December 2002 and the summer month June 2001 are evaluated. Nested Polar MM5 simulations at 24-km resolution are available for comparison. The study motivated several improvements to Polar WRF. The Noah land surface model was adjusted by setting snow–ice emissivity at 0.98 and snow–ice albedo at 0.80, treating snow cover as part of the prognostic subsurface layers, and setting snowpack heat transfer and heat storage quantities based on Yen (1981). Furthermore, initial subsurface temperatures were adapted from previous Polar MM5 simulations.

The Polar WRF simulations for December 2002 simulations show similar forecast skill to Polar MM5 simulations in comparison to automatic weather station observations. The WRF single-moment 5-class microphysics, Noah LSM, and MYJ boundary layer parameterization were selected after comparing several options. The WRF simulations have increased downward longwave radiation in contrast to the known deficit for the Polar MM5 simulations.

The June 2001 WRF simulation shows slightly less forecast skill when compared with the Polar MM5 simulation for AWS-observed variables. The surface energy balance, however, is superior for the WRF simulation. For this month, diurnal cycles of temperature and wind speed are pronounced but synoptic variability is weaker than December. Further model development will be required over different Arctic surface types including sea ice and nonfrozen land surfaces to address land surface issues and cloud-radiative properties. Testing is also required for the Antarctic region, and is proceeding at NCAR in collaboration with The Ohio State University in preparation for the transition of AMPS to Polar WRF.

Acknowledgments. This research is supported by NSF Grant 0733023, NASA Award NNG04GM26G, NOAA CIFAR Grant UAF04-0047, and UCAR Subcontract S01-22961. We thank Jason Box for access and helpful discussions about the Greenland AWS and radiation observations. Additional thanks are given to Le-Sheng Bai, who performed the Polar MM5 simulations and Lin Li who assisted with the WRF simulations. We thank John Cassano, Kevin Manning, Jordan Powers, Hugh Morrison, and Greg Thompson for insightful conversations on polar mesoscale simulations and an anonymous reviewer for helpful comments on the manuscript.

REFERENCES

Albert, M. R., and E. F. Shultz, 2002: Snow and firn properties and air–snow transport processes at Summit, Greenland. *Atmos. Environ.,* **36,** 2789–2797.

Barker, D. M., W. Huang, Y.-R. Guo, and A. Bourgeois, 2003: A three-dimensional variational (3DVAR) data assimilation system for use with MM5. NCAR Tech. Note NCAR/TN-453+STR, 68 pp. [Available from UCAR Communications, P.O. Box 3000, Boulder, CO 80307.]

——, ——, ——, ——, and X. N. Xiao, 2004: A three-dimensional variational data assimilation system for MM5: Implementation and initial results. *Mon. Wea. Rev.,* **132,** 897–914.

Bourgeois, C. S., P. Calanca, and A. Ohmura, 2006: A field study of the hemispherical directional reflectance factor and spectral albedo of dry snow. *J. Geophys. Res.,* **111,** D20108, doi:10.1029/2006JD007296.

Box, J. E., and A. Rinke, 2003: Evaluation of Greenland ice sheet surface climate in the HIRHAM regional climate model using automatic weather station data. *J. Climate,* **16,** 1302–1319.

——, D. H. Bromwich, and L.-S. Bai, 2004: Greenland ice sheet surface mass balance 1991–2000: Application of Polar MM5 mesoscale model and in situ data. *J. Geophys. Res.,* **109,** D16105, doi:10.1029/2003JD004451.

——, and Coauthors, 2006: Greenland ice sheet surface mass balance variability (1988–2004) from calibrated Polar MM5 output. *J. Climate,* **19,** 2783–2800.

Bromwich, D. H., J. J. Cassano, T. Klein, G. Heinemann, K. M. Hines, K. Steffen, and J. E. Box, 2001: Mesoscale modeling of katabatic winds over Greenland with the Polar MM5. *Mon. Wea. Rev.,* **129,** 2290–2309.

——, A. J. Monaghan, J. G. Powers, J. J. Cassano, H.-L. Wei, Y.-H. Kuo, and A. Pellegrini, 2003: Antarctic Mesoscale Prediction System (AMPS): A case study from the 2000–01 field season. *Mon. Wea. Rev.,* **131,** 412–434.

——, ——, and Z. Guo, 2004: Modeling the ENSO modulation of Antarctic climate in the late 1990s with the Polar MM5. *J. Climate,* **17,** 109–132.

——, L. Bai, and G. G. Bjarnason, 2005a: High-resolution regional climate simulations over Iceland using Polar MM5. *Mon. Wea. Rev.,* **133,** 3527–3547.

——, E. R. Toracinta, R. J. Oglesby, J. L. Fastook, and T. J. Hughes, 2005b: LGM summer climate on the southern margin of the Laurentide Ice Sheet: Wet or dry? *J. Climate,* **18,** 3317–3338.

Caplan, P., and H. L. Pan, 2000: Changes to the 1999 NCEP operational MRF analysis/forecast system. NWS Tech. Procedures Bull. 452, National Oceanic and Atmospheric Administration, 15 pp. [Available online at http://www.weather.gov/om/tpb/452.htm.]

Cassano, J. J., J. E. Box, D. H. Bromwich, L. Li, and K. Steffen, 2001: Evaluation of Polar MM5 simulations of Greenland's atmospheric circulation. *J. Geophys. Res.,* **106,** 33 867–33 889.

Chen, F., and J. Dudhia, 2001: Coupling an advanced land surface–hydrology model with the Penn State–NCAR MM5 modeling system. Part I: Model and implementation and sensitivity. *Mon. Wea. Rev.,* **129,** 569–585.

Chou, M.-D., and M. J. Suarez, 1994: An efficient thermal infrared radiation parameterization for use in general circulation models. NASA Tech. Memo. 104606, 85 pp.

Cooper, W. A., 1986: Ice initiation in natural clouds. *Precipitation Enhancement—A Scientific Challenge, Meteor. Monogr.,* No. 21, Amer. Meteor. Soc., 29–32.

Dudhia, J., 1993: A nonhydrostatic version of the Penn State–NCAR mesoscale model: Validation tests and simulation of an Atlantic cyclone and cold front. *Mon. Wea. Rev.,* **121,** 1493–1513.

Durre, I., R. S. Vose, and D. B. Wuertz, 2006: Overview of the Integrated Global Radiosonde Archive. *J. Climate,* **19,** 53–68.

Ekholm, S., 1996: A full coverage, high-resolution topographic model of Greenland computed from a variety of digital elevation data. *J. Geophys. Res.,* **101,** 21 961–21 972.

Fletcher, N. H., 1962: *The Physics of Rain Clouds.* Cambridge University Press, 386 pp.

Grell, G. A., J. Dudhia, and D. R. Stauffer, 1995: A description of the fifth-generation Penn State/NCAR mesoscale model (MM5). NCAR Tech. Note NCAR/TN-3981+STR, 122 pp.

Guo, Z., D. H. Bromwich, and J. J. Cassano, 2003: Evaluation of Polar MM5 simulations of Antarctic atmospheric circulation. *Mon. Wea. Rev.,* **131,** 384–411.

Heidam, N. Z., P. Wåhlin, and J. H. Christensen, 1999: Tropospheric gases and aerosols in northeast Greenland. *J. Atmos. Sci.,* **56,** 261–278.

Heinemann, G., 1997: Idealized simulations of the Antarctic katabatic wind system with a three-dimensional mesoscale model. *J. Geophys. Res.,* **102,** 13 825–13 834.

Hines, K. M., D. H. Bromwich, and R. I. Cullather, 1997a: Evaluating moist physics for Antarctic mesoscale simulations. *Ann. Glaciol.,* **25,** 282–286.

——, ——, and Z. Liu, 1997b: Combined global climate model and mesoscale model simulations of Antarctic climate. *J. Geophys. Res.,* **102,** 13 747–13 760.

Holland, M. M., and C. M. Bitz, 2003: Polar amplification of climate change in coupled models. *Climate Dyn.,* **21,** 221–232.

Hong, S.-Y., and H.-L. Pan, 1996: Nonlocal boundary layer vertical diffusion in a medium-range forecast model. *Mon. Wea. Rev.,* **124,** 2322–2339.

——, J. Dudhia, and S.-H. Chen, 2004: A revised approach to ice microphysical processes for the bulk parameterization of clouds and precipitation. *Mon. Wea. Rev.,* **132,** 103–120.

——, Y. Noh, and J. Dudhia, 2006: A new vertical diffusion package with an explicit treatment of entrainment processes. *Mon. Wea. Rev.,* **134,** 2318–2341.

Houghton, J. T., Y. Ding, D. J. Griggs, M. Noguer, P. J. van der Linden, X. Dai, K. Maskell, and C. A. Johnson, Eds., 2001: *Climate Change 2001: The Scientific Basis.* Cambridge University Press, 881 pp.

Janjić, Z. I., 1994: The step-mountain eta coordinate model: Further developments of the convection, viscous sublayer, and turbulence closure schemes. *Mon. Wea. Rev.,* **122,** 927–945.

——, 1996: The surface layer in the NCEP Eta Model. Preprints, *11th Conf. on Numerical Weather Prediction,* Norfolk, VA, Amer. Meteor. Soc., 354–355.

——, 2002: Nonsingular implementation of the Mellor–Yamada level 2.5 scheme in the NCEP Meso model. NCEP Office Note 437, National Centers for Environmental Prediction, 61 pp.

Kattsov, V. M., and Coauthors, 2004: Future climate change: Modeling and scenarios for the Arctic. *Arctic Climate Impact Assessment,* C. Symon, L. Arris, and B. Heal, Eds., Cambridge University Press, 99–150.

Klein, T., G. Heinemann, D. H. Bromwich, J. J. Cassano, and K. M. Hines, 2001: Mesoscale modeling of katabatic winds over Greenland and comparisons with AWS and aircraft data. *Meteor. Atmos. Phys.,* **78,** 115–132.

Lynch, A. H., W. L. Chapman, J. E. Walsh, and G. Weller, 1995: Development of a regional climate model of the Western Arctic. *J. Climate,* **8,** 1555–1570.

Mahrt, L., and M. Ek, 1984: The influence of atmospheric stability on potential evaporation. *J. Climate Appl. Meteor.,* **23,** 222–234.

——, and D. Vickers, 2005: Moisture fluxes over snow with and without protruding vegetation. *Quart. J. Roy. Meteor. Soc.,* **131,** 1251–1270.

Manabe, S., and R. J. Stouffer, 1980: Sensitivity of a global climate model to an increase of CO_2 concentration in the atmosphere. *J. Geophys. Res.,* **85,** 5529–5554.

Manning, K. W., and C. A. Davis, 1997: Verification and sensitivity experiments for the WISP94 MM5 forecasts. *Wea. Forecasting,* **12,** 719–735.

McBean, G., and Coauthors, 2004: Arctic climate: Past and present. *Arctic Climate Impact Assessment,* C. Symon, L. Arris, and B. Heal, Eds., Cambridge University Press, 21–60.

Michalakes, J., J. Dudhia, D. Gill, J. Klemp, and W. Skamarock, 1999: Design of a next generation regional weather research and forecast model. *Towards Teracomputing,* W. Zwieflhofer, Ed., World Scientific, 117–124.

——, ——, ——, T. Henderson, J. Klemp, W. Skamarock, and W. Wang, 2004: The weather research and forecast model: Software architecture and performance. *Proc. 11th ECMWF Workshop on the Use of High Performance Computing in Meteorology,* Reading, United Kingdom, European Centre for Medium-Range Weather Forecasts, 156–158.

Mlawer, E. J., S. J. Taubman, P. D. Brown, M. J. Iacono, and S. A. Clough, 1997: Radiative transfer for inhomogeneous atmosphere: RRTM, a validated correlated-*k* model for the longwave. *J. Geophys. Res.,* **102,** 16 663–16 682.

Ohmura, A., 2001: Summit Greenland environment observatory. *Mem. Nat. Inst. Polar Res.,* **54** (Special Issue), 153–159.

Overland, J., J. Calder, F. Fetterer, D. McGuire, J. Morison, J. Richter-Menge, N. Soreide, and J. Walsh, 2003: SEARCH workshop on large-scale atmosphere–cryosphere observations. *Bull. Amer. Meteor. Soc.,* **84,** 1077–1082.

Parish, T. R., and K. T. Waight III, 1987: The forcing of Antarctic katabatic winds. *Mon. Wea. Rev.,* **115,** 2214–2226.

Pinto, J. O., J. A. Curry, and C. W. Fairall, 1997: Radiative characteristics of the Arctic atmosphere during spring as inferred from ground-based measurements. *J. Geophys. Res.,* **102,** 6941–6952.

Powers, J. G., A. J. Monaghan, A. M. Cayette, D. H. Bromwich, Y.-H. Kuo, and K. W. Manning, 2003: Real-time mesoscale

modeling over Antarctica: The Antarctic Mesoscale Prediction System. *Bull. Amer. Meteor. Soc.,* **84,** 1533–1545.

Reisner, J., R. M. Rasmussen, and R. T. Bruintjes, 1998: Explicit forecasting of supercooled liquid water in winter storms using the MM5 mesoscale model. *Quart. J. Roy. Meteor. Soc.,* **124,** 1071–1107.

Rignot, E., and P. Kanagaratnam, 2006: Changes in the velocity structure of the Greenland ice sheet. *Science,* **311,** 986–990.

Serreze, M. C., M. P. Clark, and D. H. Bromwich, 2003: Monitoring precipitation over the Arctic terrestrial drainage system: Data requirements, shortcomings, and applications of atmospheric reanalysis. *J. Hydrometeor.,* **4,** 387–407.

Skamarock, W. C., J. B. Klemp, J. Dudhia, D. O. Gill, D. M. Barker, W. Wang, and J. G. Powers, 2005: A description of the advanced research WRF version 2. NCAR Tech. Note NCAR/TN–468+STR, 88 pp.

Smirnova, T. G., J. M. Brown, and S. G. Benjamin, 1997: Performance of different soil model configurations in simulating ground surface temperature and surface fluxes. *Mon. Wea. Rev.,* **125,** 1870–1884.

——, ——, ——, and D. Kim, 2000: Parameterization of cold-season processes in the MAPS land-surface scheme. *J. Geophys. Res.,* **105,** 4077–4086.

Stearns, C. R., G. A. Weidner, and L. M. Keller, 1997: Atmospheric circulation around the Greenland Crest. *J. Geophys. Res.,* **102,** 13 801–13 812.

Steffen, K., and J. E. Box, 2001: Surface climatology of the Greenland ice sheet: Greenland Climate Network 1995–1999. *J. Geophys. Res.,* **106,** 33 951–33 964.

Thompson, G., R. M. Rasmussen, and K. Manning, 2004: Explicit forecasts of winter precipitation using an improved bulk microphysics scheme. Part I: Description and sensitivity analysis. *Mon. Wea. Rev.,* **132,** 519–542.

Van Lipzig, N. P. M., E. van Meijgaard, and J. Oerlemans, 1999: Evaluation of a regional atmospheric model using measurements of surface heat exchange processes from a site in Antarctica. *Mon. Wea. Rev.,* **127,** 1994–2011.

Velicogna, I., and J. Wahr, 2006: Acceleration of Greenland ice mass loss in spring 2004. *Nature,* **443,** 329–331.

Wild, M., P. Calanca, S. C. Scherrer, and A. Ohmura, 2003: Effects of polar ice sheets on global sea level in high-resolution greenhouse scenarios. *J. Geophys. Res.,* **108,** 4165, doi:10.1029/2002JD002451.

Yen, Y. C., 1981: Review of thermal properties of snow, ice, and sea ice. Cold Regions Research and Engineering Lab (CRREL) Rep. 81-10, 27 pp.